Meteotsunami observed by the deep-ocean seafloor pressure gauge network off northeastern Japan

Tatsuya Kubota[1], Tatsuhiko Saito[1], Naotaka Yamamoto Chikasada[2], and Osamu Sandanbata[3]

[1]National Research Institute for Earth Science and Disaster Resilience
[2]National Research Institute for Earth Science and Disaster Prevention
[3]Now at National Research Institute for Earth Science and Disaster Prevention

November 24, 2022

Abstract

Recent developments in ocean-bottom pressure gauge (OBP) networks have enabled us to continuously monitor various waves in the ocean. On 1 July, 2020, an OBP network, S-net, recorded tsunami-like pressure changes, although no earthquake was reported. These waves were well explained by a numerical simulation supposing a northward-moving atmospheric low pressure system with a maximum pressure depression of -0.5 ± 0.1 hPa and an apparent speed of 100–110 m/s. This simulation suggested that these waves were meteotsunamis. The simulation also suggested that the maximum amplitudes of the sea-surface height of ˜ 2 cm were up to ˜30% larger than those expected from the observed pressure if we do not consider the effect of the atmospheric pressure change. Our study showed that the S-net can detect the generation and propagation of meteotsunamis, which could not be achieved in the past when OBP networks with only a few stations were available.

Meteotsunami observed by the deep-ocean seafloor pressure gauge network off northeastern Japan

T. Kubota[1], T. Saito[1], N. Y. Chikasada[1], and O. Sandanbata[1]

[1] National Research Institute for Earth Science and Disaster Resilience, Tsukuba, Ibaraki, Japan.

Corresponding author: Tatsuya Kubota (kubotatsu@bosai.go.jp)

Key Points:

- Deep-ocean pressure gauge array observation off NE Japan detected non-seismic tsunami-like pressure signals with amplitudes of several hPa
- A numerical simulation revealed that the signals were meteotsunamis related to a northward-moving atmospheric low pressure system
- The simulation suggests that the peak amplitude of sea-surface height of ~2 cm was up to ~30% larger than that expected from pressure data

Abstract

Recent developments in ocean-bottom pressure gauge (OBP) networks have enabled us to continuously monitor various waves in the ocean. On 1 July, 2020, an OBP network, S-net, recorded tsunami-like pressure changes, although no earthquake was reported. These waves were well explained by a numerical simulation supposing a northward-moving atmospheric low pressure system with a maximum pressure depression of −0.5 ± 0.1 hPa and an apparent speed of 100–110 m/s. This simulation suggested that these waves were meteotsunamis. The simulation also suggested that the maximum amplitudes of the sea-surface height of ~ 2 cm were up to ~30% larger than those expected from the observed pressure if we do not consider the effect of the atmospheric pressure change. Our study showed that the S-net can detect the generation and propagation of meteotsunamis, which could not be achieved in the past when OBP networks with only a few stations were available.

Plain Language Summary

Recent developments in deep-ocean tsunami observation networks have been remarkable, which have an advantage for continuously monitoring the ocean. On 1 July, 2020, a deep-ocean observation network off eastern Japan, S-net, recorded small tsunami-like ocean waves. Although tsunamis are often excited by earthquakes, no earthquake was reported at that time. Considering the features of the observed data, it is most likely that the waves were meteorological tsunamis, or meteotsunamis, originating to an atmospheric pressure system. To investigate the behavior of these waves in detail, we conducted a numerical meteotsunami simulation, and found that the meteotsunami generation source, associated with a moving atmospheric low pressure, was moving slowly northward. The maximum amplitudes of the sea-surface height were about 2 cm, which were up to ~30% larger than those expected from the observed seafloor pressure change. We demonstrated that analyzing the data from the array of wide and dense pressure gauge networks made it possible to understand the behavior of the meteotsunamis in detail, which could not be achieved in the past when only a few pressure gauges were available. The S-net's continuous monitoring of the seafloor pressure in the deep ocean will contribute to deepening our understanding of oceanography and meteorology.

1 Introduction

Recently deep-ocean tsunami observations using ocean-bottom pressure gauges (OBPs) (e.g., González et al., 2005; Tsushima & Ohta, 2014; Kaneda et al., 2015; Kawaguchi et al., 2015; Rabinobich & Eblé, 2015; Aoi et al., 2020) have been developed. Use of the deep-ocean OBPs has contributed to our understanding of earthquake rupture processes such as finite fault modeling (e.g., Kubota, Saito, Suzuki 2020) and tsunami propagation processes such as dispersion (Saito & Furumra 2009; Sandanbata et al., 2018; Kubota, Saito et al., 2020) and coastal reflection (Gusman et al. 2017; Kubota, Saito et al., 2018). In response to the 2011 Tohoku-Oki earthquake, a densely distributed OBP network consisting of 150 observatories, called the seafloor observation network for earthquakes and tsunamis along the Japan Trench (S-net), was constructed off eastern Japan (Figure 1a, Aoi et al. 2020). Recent studies have revealed that S-net is capable of observing tsunamis at much higher spatial resolutions than was previously possible. The S-net system has started to be widely utilized for monitoring waves in the ocean related to earthquakes. One of the largest tsunamis so far recorded by the S-net system was that associated with the Mw 7.0 Off-Fukushima earthquake on 21 November, 2016 (Kubota, Chikasada et al. 2020; Tsushima & Yamamoto, 2020, Figure 1d). Further, it has been reported that much smaller tsunamis with amplitudes less than one centimeter related to the Mw 6.0 Off-Iwate earthquake on 20 August, 2016 were observed by S-net (Kubota, Saito, Suzuki, 2020, Figure 1c). In addition to earthquake-induced tsunamis, or seismic tsunamis, the OBPs can record other oceanographic phenomena, such as infragravity waves and internal tides (e.g., Tonegawa et al. 2018; Fukao et al. 2019).

Here, we report new observations of tsunami-like pressure change signals recorded by S-net on 1 July, 2020 (Figure 1b, 17:00–19:00 UTC). One of the most interesting aspects of these signals is that no major earthquake, which is the most common cause of tsunamis, was reported at that time (https://www.fnet.bosai.go.jp/top.php?LANG=en). Because most current real-time tsunami forecasting methods using S-net are triggered by earthquake events (e.g., Inoue et al. 2019; Suzuki et al., 2020; Tanioka, 2020; Tsushima & Yamamoto, 2020), it will be important to investigate the source of these "non-seismic" tsunami signals in order to appropriately conduct tsunami forecasts. Therefore, we investigated the source of the observed non-seismic tsunami-like signals based on data analysis and numerical simulations. In Section 2, we summarize characteristics of the observed signals and compare them to those of tsunamis excited by earthquakes. Section 3 discusses a plausible cause of these signals. In Section 4, we conduct numerical simulations in order to clarify the cause of these tsunami-like signals and to discuss the generation and propagation processes of these waves in detail. Section 5 summarizes this research and discusses the potential use of the continuous deep-ocean pressure gauge networks.

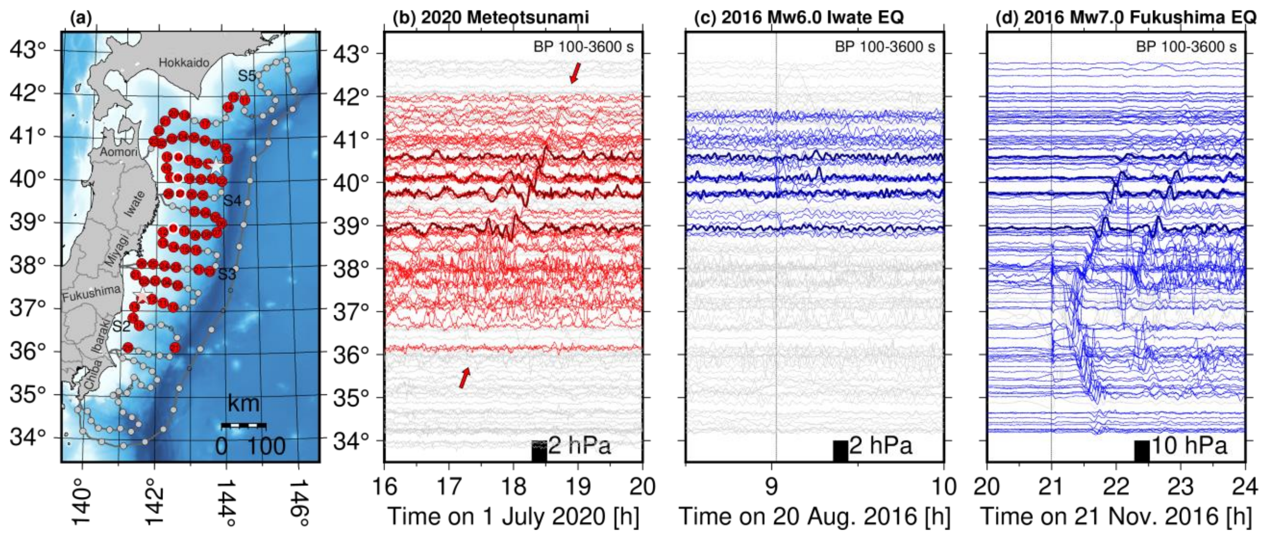

Figure 1. (a) Station map of this study. The names of prefectures are also shown. (b) Pressure waveforms recorded on 1 July 2020. The horizontal axis is the time on 1 July (UTC) and the vertical axis corresponds to the station latitude. The waveforms from the OBPs marked by white circles in Figure 1a are shown by thick lines. Data with low quality are plotted using gray lines. The tsunami-like pressure changes are denoted by red arrows. Pressure waveforms for (c) the 2016 Off-Iwate earthquake and (d) the 2016 Off-Fukushima earthquake. Epicenters for each earthquake are shown by white stars in Figure 1a. Note that horizontal scale in Figure 1c is different from the other panels.

2 S-net pressure gauge data

We analyzed the S-net OBP data for 1 July, 2020 to clarify the characteristics of the tsunami-like waves. We applied a bandpass filter with passbands of 100–3600 s to reduce noise (Figure 1b). Figure 1b shows the waveforms and indicates data with reasonable quality by (red lines). The waveforms for the different water depth bins are also shown in Figure S1: <1500 m (Figure S1a), 1500–4000 m (Figure S1b), and >4000 m (Figure S1c). We confirmed a wave train of pressure changes propagating to the north during the period 17:00–19:00 UTC (Figure

1b), which were too small to be recognized if only a few observation stations were available. The wave train emerges in the region off northern Fukushima and southern Miyagi prefectures, and disappears in the region off northern Iwate and southern Aomori prefectures. In contrast, a wave train propagating to the south could not be confirmed (34°N–37°N). We were unable to recognize waves using the OBPs installed in deeper waters (> 4000 m), particularly for the subnetwork installed in the outer-trench region (Figure S1c).

Based on the pressure waveforms for which the wave signals are evident, it seems that the dominant period T' is about ~1000–1200 s. This dominant period is almost comparable to the tsunamis associated with the Mw 7.0 Off-Fukushima earthquake (Figure 1d, Kubota, Chikasada et al., 2020; Tsushima & Yamamoto, 2020), although the maximum amplitudes of a few hectopascals are almost five times smaller than those for this earthquake (~10 hPa = 10 cmH_2O, supposing that a pressure change of 1 hPa is equivalent to a sea height change of 1 cmH_2O). On the other hand, the maximum amplitudes are similar to those for the Mw 6.0 Off-Iwate earthquake (Figure 1c), although the dominant periods for this earthquake were much shorter (~300 s, Kubota, Saito, Suzuki, 2020). These inconsistencies may also suggest that these pressure signals have a different origin to the typical tsunamis generated by earthquakes.

We plot the distributions of the peak amplitude of the seafloor pressure and its arrival times in Figure 2. The peak amplitudes are mostly a few hectopascals and tend to be large in the OBPs at shallower depths (water depth of < ~1500 m). From the peak arrival times, the apparent propagation direction of this wave train is almost northward. Using data from the OBP stations installed off Iwate Prefecture at water depths between 1000 and 1500 m (S4N14, S4N18, S4N27, and S3N11, marked by circles with thick white lines in Figure 2b), the apparent propagation velocity c' along the north-source direction is calculated as $c' = 109.2 \pm 3.7$ m/s. This apparent propagation velocity corresponds to the tsunami propagation velocity at water depths of ~1000–1200 m (e.g., Satake, 2002). Considering the dominant period and the apparent propagation velocity, the north-south extents of each region of the uplift and subsidence are inferred to be $c'T' \times 0.5 \sim 50$ km. However, based on the earthquake-fault scaling relation of Wells & Coppersmith (1994), the seismic magnitudes of earthquakes that would generate such a large horizontal tsunami source dimension would be expected to be M ~7 or larger. This unexpectedly large horizontal extent of the tsunamis is inconsistent with those induced by earthquakes.

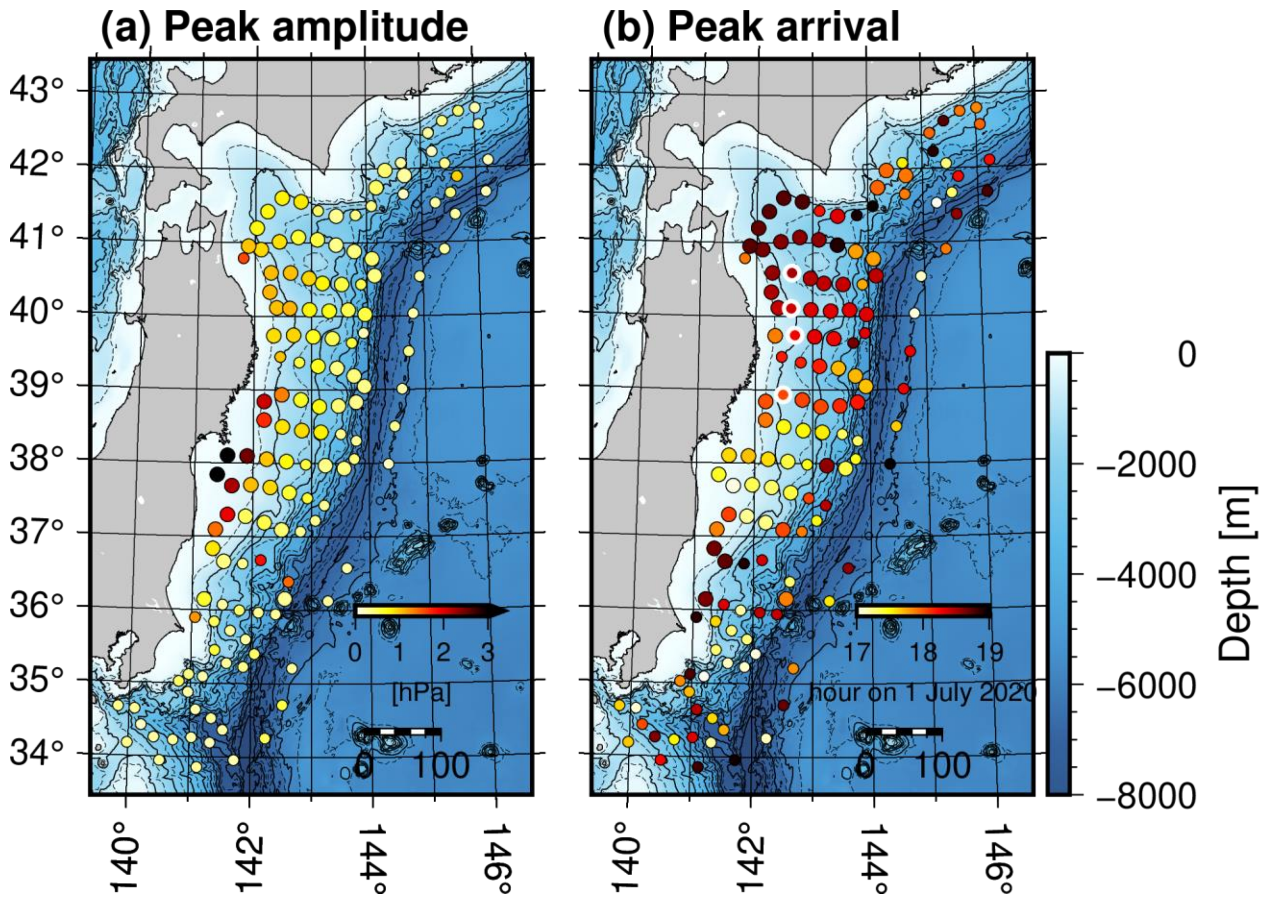

Figure 2. (a) Peak amplitudes of S-net pressure records. (b) Arrival timings of the peak amplitudes. The stations marked by thick white circles are used for calculating the apparent wave propagation velocity (see Figure 4). The pressure data in which the signal-to-noise ratio is low are indicated by small circles. The iso-depth contours are also shown. Solid and dashed contour lines are drawn at 1000 m and 500 m intervals, respectively. The color scale of the sea depth is also shown.

3 A plausible cause of the pressure signals

In addition to the seafloor crustal deformation due to earthquakes, tsunami-like ocean waves are often excited by meteorological phenomena. These waves are widely referred to as meteorological tsunamis, or meteotsunamis (Rabinovich, 2020), which are generated by the interaction between atmospheric disturbances and water-wave propagation (e.g., Hibiya & Kajiura, 1982). One of the most distinctive characteristics of meteotsunamis is that they are not accompanied by earthquakes or seismic waves. In fact, the weather map of Japan obtained when the tsunami-like wave signals occurred (http://database.rish.kyoto-u.ac.jp/arch/jmadata/) show a low pressure system moving to the east to northeast at 18:00 on July 1, 2020 (marked by a black arrow in Figures S2b). Therefore, it seems that these tsunami-like pressure changes were likely induced by meteotsunamis. The significantly large horizontal extent of the tsunamis also supports this idea.

The basic generation mechanism of a meteotsunami has been theoretically investigated (e.g., Proudman, 1929; Greenspan, 1956; An et al., 2012; Seo & Liu, 2014; Saito et al., 2021). Meteotsunamis have been widely recorded by coastal tide gauges, which have enhanced meteotsunami research (e.g., Hibiya & Kajiura 1982; Monserrat et al. 2006; Seo & Liu, 2014; Šepić et al. 2015; Williams et al. 2019; Fukuzawa & Hibiya, 2020; Heidarzadeh, Šepić et al. 2020; Rabinovich et al. 2020; Okal 2020). However, meteotsunami observations in the deep-ocean have been reported much less (Titov & Moore, 2021). In the next section, we conduct numerical simulations of meteotsunamis in order to confirm whether the observed wave train was due to a meteotsunami, and to investigate the behavior of meteotsunamis in the open ocean.

4 Meteotsunami simulation in the region off eastern Japan

4.1 Method

The equation for meteotsunami propagation is given by adding an external force term related to the atmospheric pressure to tsunami equations (e.g., Satake, 2002). In this study, we introduce a linear-long wave equation in Cartesian coordinates (e.g., Hibiya & Kajiura, 1982; An et al., 2012):

$$\frac{\partial \eta}{\partial t} + \frac{\partial M}{\partial x} + \frac{\partial N}{\partial y} = 0$$

$$\rho_0 \frac{1}{h}\frac{\partial M}{\partial t} + \rho_0 g_0 \frac{\partial \eta}{\partial x} = -\frac{\partial p_{\mathrm{atm}}}{\partial x}, \qquad (1)$$

$$\rho_0 \frac{1}{h}\frac{\partial N}{\partial t} + \rho_0 g_0 \frac{\partial \eta}{\partial y} = -\frac{\partial p_{\mathrm{atm}}}{\partial y}$$

where $\eta(x, y, t)$ is the sea-surface height change and $M(x, y, t)$ and $N(x, y, t)$ are the vertically integrated horizontal velocity from the seafloor to the sea surface along the *x*- and *y*- directions, respectively. Parameter h is the seawater depth, g_0 is the gravity acceleration (= 9.8 m/s^2) and ρ_0

is the seawater density. We suppose the seawater density to be $\rho_0 = 1020\ \mathrm{kg/m^3}$, so that a pressure change of 1 hPa is equivalent to a sea-height change of 1 cm (i.e., $\rho_0 g_0 = 1\ \mathrm{hPa/cm}$). In the numerical simulation, we use the bathymetry data of GEBCO 2019 Grid (https://www.gebco.net/data_and_products/historical_data_sets/#gebco_2019). We set the spatial grid interval as 2 km and the time step interval as 1 s.

As the atmospheric pressure disturbance, we suppose a plane-wave of the low-pressure system moving northward (azimuth of $\phi_p = 0°$) with a speed of V_0. Introducing the Cartesian coordinate in which the *x*- and *y*-directions coincide with the east and north directions, respectively, the spatiotemporal evolution of the atmospheric pressure is given by

$$p_{\mathrm{atm}}(x, y, t) = p_1(x, y, t)\tau(t) = P_0 \exp\left[-\left(\frac{y - V_0 t}{L_0/2}\right)^2\right]\tau(t), \tag{2}$$

where P_0 is the amplitude of the atmospheric pressure disturbance and L_0 is the horizontal extent of the plane wave. We assume that $L_0 = 50$ km, determined based on the apparent propagation velocity and the dominant period of the observed waveforms (Figure 2). Because it is unlikely that the atmospheric pressure suddenly increases at *t* = 0 s, we suppose that the moving pressure increases gradually over time with a time scale of T_0 (An et al. 2012):

$$\tau(t) = \left(1 - \exp\left[-\left(\frac{t}{T_0/2}\right)^2\right]\right). \tag{3}$$

We suppose the duration of this increase to be $T_0 = 5400$ s. We vary the moving speed V_0 of the plane wave and its amplitude P_0 to find optimal values for the two parameters by comparing the simulated and observed waves, particularly in terms of the apparent propagation velocity and the amplitude.

In order to calculate the pressure change at the sea bottom $p_{\mathrm{bot}}(x, y, t)$, we consider the pressure changes due to tsunami $p_{\mathrm{eta}}(x, y, t)$ and the atmospheric pressure disturbance $p_{\mathrm{atm}}(x, y, t)$, to be as follows (e.g., Inazu et al., 2012; Saito et al., 2021):

$$p_{\mathrm{bot}}(x, y, t) = p_{\mathrm{eta}}(x, y, t) + p_{\mathrm{atm}}(x, y, t). \tag{4}$$

Here, the pressure changes due to tsunamis are expressed as:

$$p_{\mathrm{eta}}(x,y,t) = \rho_0 g_0 \eta(x,y,t). \quad (5)$$

4.2 Results and interpretations

In Figure 3, we show the meteotsunami simulation result with $V_0 = 110\ \mathrm{m/s}$ and $P_0 = -0.5$ hPa, which explains best the observed pressure changes among the simulations we conducted. Figures 3a to 3d show snapshots of the atmospheric pressure (left panels), sea-surface height (middle panels), and the seafloor pressure (right panels). The sea-surface subsidence and the seafloor pressure decrease propagates to the north as the leading wave in which the amplitudes grow gradually in the region closest to the coast (marked by blue arrows in Figure 3). The dominant sea-surface uplift follows the leading wave (red arrows in Figure 3). This uplift extends widely in the east-west direction, corresponding to the region of the atmospheric low pressure (black arrows in Figure 3), whereas seafloor pressure increases are confirmed only in the region near the coast. This is due to the hydrostatic equilibrium, in which the pressure change by the sea-surface uplift is cancelled by the atmospheric pressure coast (gray arrows in Figure 3).

Figure 3e shows a comparison of the simulated pressure waveforms at the OBPs with the observations (left panel). To visualize more clearly the characteristics of the apparent arrival delays of the wave packets, we plot its envelope waveforms (right panel in Figure 3e). The arrival timings of the peak amplitudes are explained well. We obtain the apparent propagation velocity along the north-south direction as $c' = 110.4 \pm 2.3\ \mathrm{m/s}$. This is consistent with the observed data. From this simulation, we conclude that these tsunami-like pressure changes are meteotsunamis excited by a moving low pressure system.

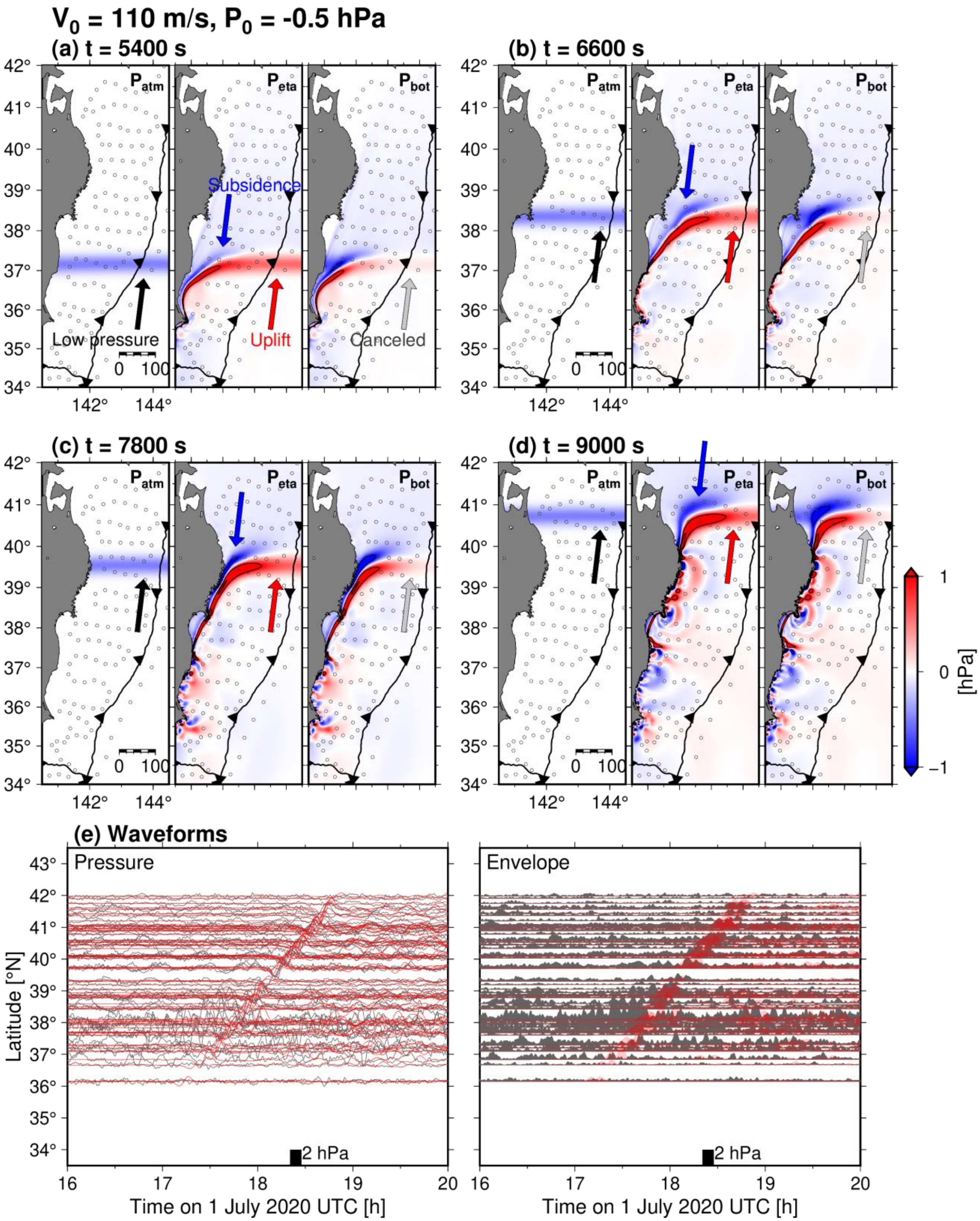

Figure 3. Result of the meteotsunami simulation supposing northward moving atmospheric pressure with V_0 = 110 m/s. Snapshots of the simulations at elapsed times of (a) 5400, (b) 6600, (c) 7200, and (d) 8400 s are shown. In each subfigure, the pressure changes due to the

atmosphere disturbance (left), sea-surface height (middle), and sea-bottom pressure (right) are shown. (e) Comparison of the observed and simulated bottom pressure waveforms. The pressure waveforms and the envelope waveforms are shown in left and right panels, respectively.

When assuming an atmospheric low pressure moving slower (V_0 = 50 m/s, Figure S3) or faster (200 m/s, Figure S4) than the optimum value ($V_0 = 110$ m/s), neither simulation could explain the observed apparent propagation velocity. To evaluate the movement speed in further detail, we calculated apparent propagation velocities of the meteotsunamis from the simulations using atmospheric pressures moving at different speeds (Figure 4). When V_0 is assumed to be 105 or 110 m/s, the peak arrival timings of the observed pressure changes are explained (red solid lines), while the simulations with faster ($V_0 \geq$ 115 m/s) or slower ($V_0 \leq$ 100 m/s) movement speeds do not (thin red dashed lines), which suggests that the apparent northward movement speed of the low pressure region is V_0 ~105–110 m/s.

When the movement speed of the atmospheric disturbance V_0 and the phase velocity of the tsunami propagation c_0 are almost equal ($V_0 \sim c_0$), the amplitudes increase gradually (e.g., Proudman, 1929). This mechanism is often referred to as the Proudman effect, or Proudman resonance (e.g., Heidarzadeh, Šepić et al., 2020; Rabinovich, 2020). Since the tsunami propagation velocity c_0 is approximately given by $c_0 = \sqrt{g_0 h_0}$ supposing a long-wave appoximation (e.g., Satake, 2002), the meteorological tsunami observed by S-net was considered to be generated at a depth of $h_0 \sim 1200$ m.

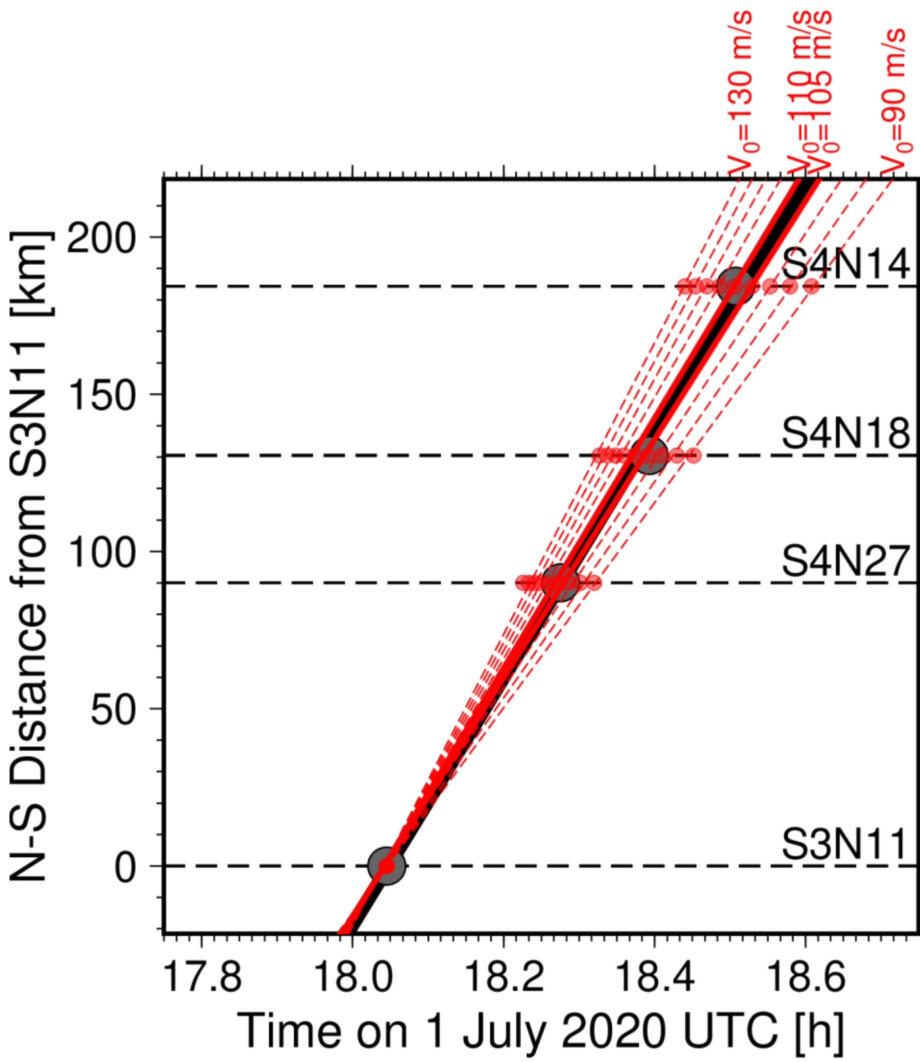

Figure 4. Comparisons of the peak timing for the OBPs. Gray circles and the black line denote the observed timing of the peak arrivals and its linear fitting function. Those for the meteotsunami simulations are denoted by red circles and lines. In the simulated results, the movement speeds of the atmospheric pressure change are varied by 5 m/s intervals. Arrival timings in the simulation are aligned so that the simulated arrivals at S3N11 coincide with the observations.

Figure 5a compares the observed (black) and simulated pressure changes at representative OBP stations. The amplitude of the atmospheric pressure disturbance supposing $P_0 = -0.5$ hPa, explains the observed amplitudes well (red traces). The peak-to-peak amplitudes of the pressure changes for the observation and simulation are 2.0 and 2.1 hPa at S4N14, 2.4 and 2.3 hPa at S4N18, 2.2 and 2.1 hPa at S4N27, and 2.5 and 2.2 hPa at S3N11, respectively. If we assume $P_0 = -1.0$ hPa (pink dash-and-dot traces in Figure 5a) or $P_0 = -0.2$ hPa (dark red dashed traces), then the simulated amplitudes are not consistent with the observations. If we assume a range between 80 and 120% of the observed peak-to-peak amplitude at S4N27, the plausible amplitude range of atmospheric pressure disturbance is estimated as P_0 ~0.5 ± 0.1 hPa.

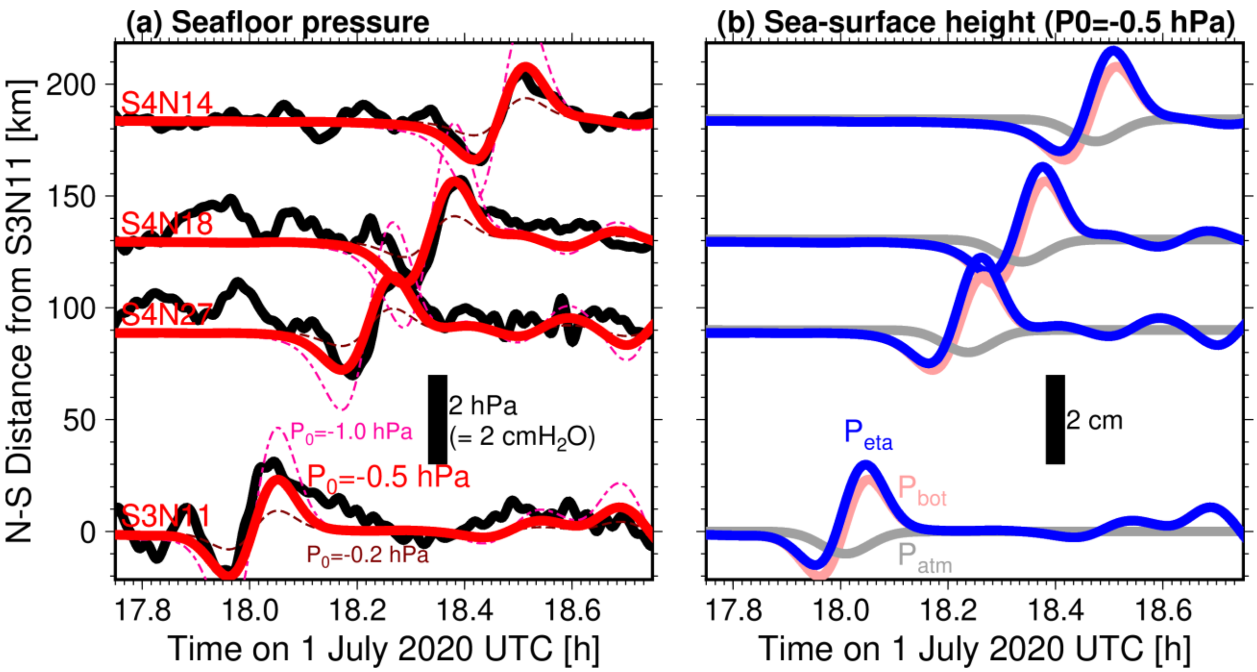

Figure 5. (a) Comparison of the observed and simulated pressure changes. Black traces are the observed pressure changes. Red thick traces are the simulated waveforms supposing $P_0 = -0.5$ hPa. The simulations with $P_0 = -1.0$ hPa and -0.2 hPa are shown by pink dash-and-dotted lines and by dark read dashed lines, respectively. (b) Time series of the sea-surface height changes simulated from the optimum simulation results (blue traces). Light pink traces are the simulated pressure changes, which are identical to the red traces in Figure 5a. Gray traces are the atmospheric pressure changes.

Considering Eq. (4), the OBPs observe the pressure changes at the seafloor (p_{bot}), but not the sea-surface height (p_{eta}). Using the simulation results, we calculated the time series of the sea-surface height changes (blue traces in Figure 5b). At station S4N27, the peak amplitude of the seafloor pressure change was 1.2 hPa, while the maximum sea-surface height was 1.6 cm (corresponding to a bottom pressure change of 1.6 hPa). In other words, the maximum amplitude of the sea-surface height was approximately 1.3 times larger than that expected from the observed seafloor pressure, without considering the atmospheric low pressure, $p_{\mathrm{bot}} = p_{\mathrm{eta}}$. Similar features were also observed for the other OBPs in Figure 5. This suggests the seafloor pressure changes p_{bot} cannot be directly converted to the sea-surface heights η, as has often been done in analyses of earthquake-induced tsunamis that are not affected by the atmospheric pressure at the sea-surface (e.g., Kubota, Saito, Suzuki, 2020). For meteotsunamis, we should consider the effect of the atmospheric pressure to appropriately estimate the sea-surface height.

We also conducted a meteotsunami simulation, supposing that the pressure disturbance moved northeastward ($\phi_p = 60°$) with a speed of $V_0 = 55\ \mathrm{m/s}$ (Figure S5). The result also explains the apparent arrivals of the observed pressure (Figure S5e). In this case, the apparent speed of the moving pressure toward the north is $V_{\mathrm{apparent}} = V_0/\cos\phi_p = 110\ \mathrm{m/s}$, which is identical to the optimum value in the simulation assuming a northward-moving low pressure. Although the seafloor bathymetry has a slope in the coast-perpendicular direction in this region, the water depth is almost uniform along the coast-parallel direction in this region, possibly causing a Proudman resonance. This simulation indicates that the apparent velocity along the north-south direction is more important for meteotsunami generation in the region off eastern Japan than the actual movement speed and direction. This kind of meteotsunami is often referred to as a Greenspan resonance (Greenspan, 1956; Munk, 1956). A Greenspan resonance occurs when the coast-parallel component of the atmospheric moving speed equals the phase velocity of the tsunami edge waves, which results in a meteotsunami due to coastally trapped edge waves.

We finally compared the meteorological observation with our results. A mesoscale weather map during the meteotsunami (http://database.rish.kyoto-u.ac.jp/arch/jmadata/) is shown in Figure S2. As mentioned in Section 3, the low pressure region moving to the northeast to east of Japan was confirmed (black arrow in Figures S2). The meteorological observations also support the hypothesis that these pressure waves are meteotsunamis, although it is difficult to measure the apparent northward movement speed of the low pressure region from this weather map.

5 Discussion and Conclusions

On July 1, 2020, the S-net OBP network recorded tsunami-like changes in pressure signals, although no earthquake event was reported. We first summarized the characteristics of the observed records, and we supposed that the most plausible sources of these pressure change signals were meteotsunamis. We then conducted numerical simulations of the meteotsunami to confirm whether these pressure changes were a meteotsunami. The simulation results showed an apparent delay in the arrival of the observed signals based on the assumption of a northward-moving atmospheric pressure disturbance with a speed of 105–110 m/s and a maximum pressure depression of −0.5 ± 0.1 hPa. This additional tsunami simulation also suggested that the apparent speed of the moving pressure system in a north-south direction is important for meteotsunami generation in the Off-eastern Japan region. We also found that the change in the peak amplitude of the sea-surface height was up to 1.3 times larger than that expected from the observed seafloor if we do not consider the atmospheric pressure change at the sea-surface. This indicates that the seafloor pressure p_{bot} cannot be directly converted to the sea-surface height η, as is often done in seismic tsunami observations, and that we need to consider the contribution of the atmospheric pressure p_{eta}.

Our study revealed that the S-net seafloor OBP network can detect the generation and propagation of meteotsunamis off eastern Japan, which could not be achieved in the past when OBP networks with only a few stations were available. So far, meteotsunami observations have mostly depended on near-shore data recorded by coastal tide gauges or seafloor pressure gauges inside bays (Rabinovich, 2020); however, these regions are typically characterized by complex coastal site effects, making it difficult to study the generation and propagation processes of meteotsunamis. In contrast, deep-ocean OBP networks are free from such near-shore site effects. Our study demonstrated that the S-net system can contribute to research on meteotsunamis and other meteorological and oceanographic studies.

Data Availability Statement

The S-net pressure gauge data is available at the website of the National Research Institute for Earth Science and Disaster Resilience (NIED) (NIED, 2019; https://doi.org/10.17598/NIED.0007). The GEBCO2019 Grid bathymetry data are available at https://www.gebco.net/data_and_products/historical_data_sets/. The atmospheric pressure data of the Meso-scale model (MSM) in Figure S2 were downloaded at http://database.rish.kyoto-u.ac.jp/arch/jmadata/ (in Japanese), and are originally provided by the Japan Meteorological Business Support Center (http://www.jmbsc.or.jp/en/index-e.html). We used Seismic Analysis Code (SAC) software for data processing (Goldstein et al., 2003). The F-net earthquake mechanism catalog (Fukuyama et al., 1998) is available at https://www.fnet.bosai.go.jp/top.php?LANG=en. Figures were prepared using Generic Mapping Tools Version 6 (GMT6) software (Wessel et al., 2019).

Acknowledgments, Samples, and Data

This work was financially supported by JSPS KAKENHI Grant Numbers JP19H02409 and JP19K14818 from the Japan Society for the Promotion of Science. We thank Yuusuke Tanaka of Japan Agency for Marine-Earth Science and Technology for the comments and discussions. The English in this manuscript was edited by Forte Science Communications (www.forte-science.co.jp)

References

An, C., Liu, P. L. F., & Seo, S. N. (2012). Large-scale edge waves generated by a moving atmospheric pressure. *Theoretical and Applied Mechanics Letters*, *2*(4), 042001. https://doi.org/10.1063/2.1204201

Aoi, S., Asano, Y., Kunugi, T., Kimura, T., Uehira, K., Takahashi, N., & Ueda, H. (2020). MOWLAS : NIED observation network for earthquake , tsunami and volcano. *Earth, Planets and Space*, *72*, 126. https://doi.org/10.1186/s40623-020-01250-x

Bryant, E. (2008). *Tsunami: the underrated hazard* (2nd ed.). Cambridge: Cambridge University Press. https://doi.org/10.1007/978-3-540-74274-6

Fukao, Y., Miyama, T., Tono, Y., Sugioka, H., Ito, A., Shiobara, H., … Miyazawa, Y. (2019). Detection of ocean internal tide source oscillations on the slope of Aogashima Island, Japan. *Journal of Geophysical Research: Oceans*, *124*, 4918–4933. https://doi.org/10.1029/2019jc014997

Fukuyama, E., Ishida, M., Dreger, D. S., & Kawai, H. (1998). Automated seismic moment tensor determination by using on-line broadband seismic waveforms. *Zisin 2*, *51*, 149–156 (in Japanese with English abstract). https://doi.org/10.4294/zisin1948.51.1_149

Fukuzawa, K., & Hibiya, T. (2020). The amplification mechanism of a meteo-tsunami originating off the western coast of Kyushu Island of Japan in the winter of 2010. *Journal of Oceanography*, *76*, 169–182. https://doi.org/10.1007/s10872-019-00536-3

Goldstein, P., Dodge, D. , Firpo, M., & Minner L. (2003). SAC2000: Signal processing and analysis tools for seismologists and engineers. In: W. H. K. Lee, H. Kanamori, P. C. Jennings, & C. Kisslinger (Eds.), *International Handbook of Earthquake and Engineering Seismology* (Vol. 81(B), pp. 1613–1614). London: Academic Press. https://doi.org/10.1016/S0074-6142(03)80284-X

González, F. I., Bernard, E. N., Meinig, C., Eble, M. C., Mofjeld, H. O., & Stalin, S. (2005). The NTHMP tsunameter network. *Natural Hazards*, *35*, 25–39. https://doi.org/10.1007/s11069-004-2402-4

Greenspan, H. P. (1956). The generation of edge waves by moving pressure distributions. *Journal of Fluid Mechanics*, *1*, 574–592. https://doi.org/10.1017/S002211205600038X

Gusman, A. R., Satake, K., Shinohara, M., Sakai, S., & Tanioka, Y. (2017). Fault slip distribution of the 2016 Fukushima earthquake estimated from tsunami waveforms. *Pure and Applied Geophysics*, *174*, 2925–2943. https://doi.org/10.1007/s00024-017-1590-2

Heidarzadeh, M., Šepić, J., Rabinovich, A., Allahyar, M., Soltanpour, A., & Tavakoli, F. (2020). Meteorological Tsunami of 19 March 2017 in the Persian Gulf: Observations and Analyses. *Pure and Applied Geophysics*, *177*, 1231–1259. https://doi.org/10.1007/s00024-019-02263-8

Hibiya, T., & Kajiura, K. (1982). Origin of the Abiki phenomenon (a kind of seiche) in Nagasaki Bay. *Journal of the Oceanographical Society of Japan*, *38*, 172–182. https://doi.org/10.1007/BF02110288

Inazu, D., Hino, R., & Fujimoto, H. (2012). A global barotropic ocean model driven by synoptic atmospheric disturbances for detecting seafloor vertical displacements from in situ ocean bottom pressure measurements. *Marine Geophysical Research*, *33*(2), 127–148. https://doi.org/10.1007/s11001-012-9151-7

Inoue, M., Tanioka, Y., & Yamanaka, Y. (2019). Method for near-real time estimation of Tsunami sources using ocean bottom pressure sensor network (S-net). *Geosciences*, *9*, 310. https://doi.org/10.3390/geosciences9070310

Kaneda, Y., Kawaguchi, K., Araki, E., Matsumoto, H., Nakamura, T., Kamiya, S., … Takahashi, N. (2015). Development and application of an advanced ocean floor network system for megathrust earthquakes and tsunamis. In P. Favali, L. Beranzoli, & A. De Santis (Eds.), *Seafloor Observatories: A new vision of the Earth from the Abyss* (pp. 643–662). https://doi.org/10.1007/978-3-642-11374-1_25

Kawaguchi, K., Kaneko, S., Nishida, T., & Komine, T. (2015). Construction of the DONET real-time seafloor observatory for earthquakes and tsunami monitoring. In P. Favali, L. Beranzoli, & A. De Santis (Eds.), *Seafloor Observatories: A new vision of the Earth from the Abyss* (pp. 211–228). https://doi.org/10.1007/978-3-642-11374-1_10

Kubota, T., Saito, T., Ito, Y., Kaneko, Y., Wallace, L. M., Suzuki, S., … Henrys, S. (2018). Using tsunami waves reflected at the coast to improve offshore earthquake source parameters: application to the 2016 Mw 7.1 Te Araroa earthquake, New Zealand. *Journal of Geophysical Research: Solid Earth*, *123*, 8767–8779. https://doi.org/10.1029/2018JB015832

Kubota, T., Suzuki, W., Nakamura, T., Chikasada, N. Y., Aoi, S., Takahashi, N., & Hino, R. (2018). Tsunami source inversion using time-derivative waveform of offshore pressure records to reduce effects of non-tsunami components. *Geophysical Journal International*, *215*, 1200–1214. https://doi.org/10.1093/gji/ggy345

Kubota, T., Saito, T., & Suzuki, W. (2020). Millimeter-scale tsunami detected by a wide and dense observation array in the deep ocean: Fault modeling of an Mw 6.0 interplate earthquake off Sanriku, NE Japan. *Geophysical Research Letters*, *47*, e2019GL085842. https://doi.org/10.1029/2019GL085842

Kubota, T., Saito, T., Chikasada, N. Y., & Suzuki, W. (2020). Ultrabroadband seismic and tsunami wave observation of high-sampling ocean-bottom pressure gauge covering periods from seconds to hours. *Earth and Space Science*, *7*, e2020EA001197. https://doi.org/10.1029/2020ea001197

Kubota, T., Chikasada, N. Y., Tsushima, H., Suzuki, W., Nakamura, T., & Kubo, H. (2020, July 12–16). *Tsunami analysis using the S-net pressure gauge records during the Mw 7.0 Off-Fukushima earthquake on 22 November 2016 to reduce the effects of tsunami-irrelevant pressure components* [Conference presentation]. JpGU-AGU Joint Meeting 2020, Online. https://confit.atlas.jp/guide/event/jpgu2020/subject/HDS08-11/advanced

Monserrat, S., Vilibić, I., & Rabinovich, A. B. (2006). Meteotsunamis: Atmospherically induced destructive ocean waves in the tsunami frequency band. *Natural Hazards and Earth System Science*, *6*, 1035–1051. https://doi.org/10.5194/nhess-6-1035-2006

Munk, W., Snodgrass, F., & Carrier, G. (1956). Edge waves on the continental shelf. *Science*, *123*, 127–132. https://doi.org/10.1126/science.123.3187.127

National Research Institute for Earth Science and Disaster Resilience (2019), *NIED S-net* [Data set]. National Research Institute for Earth Science and Disaster Resilience. https://doi.org/10.17598/nied.0003.

Okal, E. A. (2020). On the possibility of seismic recording of meteotsunamis. *Natural Hazards*, . https://doi.org/10.1007/s11069-020-04146-x

Proudman, J. (1929). The effects on the sea of changes in atmospheric pressure. *Geophysical Supplements to the Monthly Notices of the Royal Astronomical Society*, *2*, 197–209. https://doi.org/10.1111/j.1365-246X.1929.tb05408.x

Rabinovich, A. B., & Eblé, M. C. (2015). Deep-ocean measurements of tsunami waves. *Pure and Applied Geophysics*, *172*, 3281–3312. https://doi.org/10.1007/s00024-015-1058-1

Rabinovich, A. B. (2020). Twenty-Seven Years of Progress in the Science of Meteorological Tsunamis Following the 1992 Daytona Beach Event. *Pure and Applied Geophysics*, *177*, 1193–1230. https://doi.org/10.1007/s00024-019-02349-3

Rabinovich, A. B., Šepić, J., & Thomson, R. E. (2020). The meteorological tsunami of 1 November 2010 in the southern Strait of Georgia: a case study. *Natural Hazards*. https://doi.org/10.1007/s11069-020-04203-5

Saito, T., Matsuzawa, T., Obara, K., & Baba, T. (2010). Dispersive tsunami of the 2010 Chile earthquake recorded by the high-sampling-rate ocean-bottom pressure gauges. *Geophysical Research Letters*, *37*, L23303. https://doi.org/10.1029/2010GL045290

Saito, T., & Kubota, T. (2020). Tsunami modeling for the deep sea and inside focal areas. *Annual Review of Earth and Planetary Sciences*, *48*, 121–145. https://doi.org/10.1146/annurev-earth-071719-054845

Saito, T., Kubota, T., Chikasada, N. Y., Tanaka, Y., & Sandanbata, O. (2021). Meteorological tsunami generation due to sea-surface pressure change: Three-dimensional theory and synthetics of ocean-bottom pressure change [Preprint]. *Earth and Space Science Open Archive*. https://doi.org/10.1002/essoar.10504961.1

Sandanbata, O., Watada, S., Satake, K., Fukao, Y., Sugioka, H., Ito, A., & Shiobara, H. (2018). Ray tracing for dispersive tsunamis and source amplitude estimation based on Green's law: application to the 2015 volcanic tsunami earthquake near Torishima, south of Japan. *Pure and Applied Geophysics*, *175*, 1371–1385. https://doi.org/10.1007/s00024-017-1746-0

Satake, K. (2002). Tsunamis. In W. H. K. Lee, P. Gennings, C. Kisslinger, & H. Kanamori (Eds.), *International Handbook of Earthquake and Engineering Seismology* (pp. 437–451). London: Academic Press.

Seo S. N. & Liu, P. L. F. (2014). Edge waves generated by atmospheric pressure disturbances moving along a shoreline on a sloping beach. *Coastal Engineering*, *85*, 43–59. https://doi.org/10.1016/j.coastaleng.2013.12.002

Šepic, J., Vilibic, I., Rabinovich, A. B., & Monserrat, S. (2015). Widespread tsunami-like waves of 23-27 June in the Mediterranean and Black Seas generated by high-Altitude atmospheric forcing. *Scientific Reports*, *5*, 11682. https://doi.org/10.1038/srep11682

Suzuki, W., Kubota, T., Nakamura, T., & Chikasada, N. Y. (2020, July 12–16). *Development of automatic tsunami inversion system, Marlin* [Conference presentation]. JpGU-AGU Joint Meeting 2020, Online. https://confit.atlas.jp/guide/event/jpgu2020/subject/SCG70-08/advanced

Tanioka, Y. (2020). Improvement of near-field tsunami forecasting method using ocean bottom pressure sensor network (S-net). *Earth, Planets and Space*, *72*, 132. https://doi.org/10.1186/s40623-020-01268-1

Titov, V., & Moore, C. (2021). Meteotsunami model forecast: can coastal hazard be quantified in real time? *Natural Hazards*, (0123456789). https://doi.org/10.1007/s11069-020-04450-6

Tonegawa, T., Fukao, Y., Shiobara, H., Sugioka, H., Ito, A., & Yamashita, M. (2018). Excitation location and seasonal variation of transoceanic infragravity waves observed at an absolute pressure gauge array. *Journal of Geophysical Research: Oceans*, *123*, 40–52. https://doi.org/10.1002/2017JC013488

Tsushima, H., & Ohta, Y. (2014). Review on near-field tsunami forecasting from offshore tsunami data and onshore GNSS data for tsunami early warning. *Journal of Disaster Research*, *9*(3), 339–357. https://doi.org/10.20965/jdr.2014.p0339

Tsushima, H., & Yamamoto, T. (2020, July 12–16). *Operational use of tsunami source inversion in near-field tsunami warning by JMA* [Conference presentation]. JpGU-AGU Joint Meeting 2020, Online. https://confit.atlas.jp/guide/event/jpgu2020/subject/HDS08-12/advanced

Wells, D. L., & Coppersmith, K. J. (1994). New empirical relationships among magnitude, rupture length, rupture width, rupture area, and surface displacement. *Bulletin of the Seismological Society of America*, *84*, 974–1002.

Wessel, P., Luis, J. F., Uieda, L., Scharroo, R., Wobbe, F., Smith, W. H. F., & Tian, D. (2019). The Generic Mapping Tools Version 6. *Geochemistry, Geophysics, Geosystems*, *20*, 5556–5564. https://doi.org/10.1029/2019GC008515

Williams, D. A., Horsburgh, K. J., Schultz, D. M., & Hughes, C. W. (2019). Examination of generation mechanisms for an english channel meteotsunami: Combining observations and modeling. *Journal of Physical Oceanography*, *49*, 103–120. https://doi.org/10.1175/JPO-D-18-0161.1

AGU PUBLICATIONS

Geophysical Research Letters

Supporting Information for

Meteotsunami observed by the deep-ocean seafloor pressure gauge network off northeastern Japan

T. Kubota[1], T. Saito[1], N. Y. Chikasada[1], and O. Sandanbata[1]

[1]National Research Institute for Earth Science and Disaster Resilience, Tsukuba, Ibaraki, Japan.

Contents of this file

Figures S1 to S5

Introduction

Figure S1 shows the processed waveforms shown in different depth bins. Figure S2 shows the weather map during the meteotsunami event. The meteotsunami simulation results assuming the atmospheric disturbances with slower and faster moving speed are shown in Figures S3 and S4. In Figure S5, the meteotsunami simulation assuming the atmospheric disturbances moving to the northeast is shown.

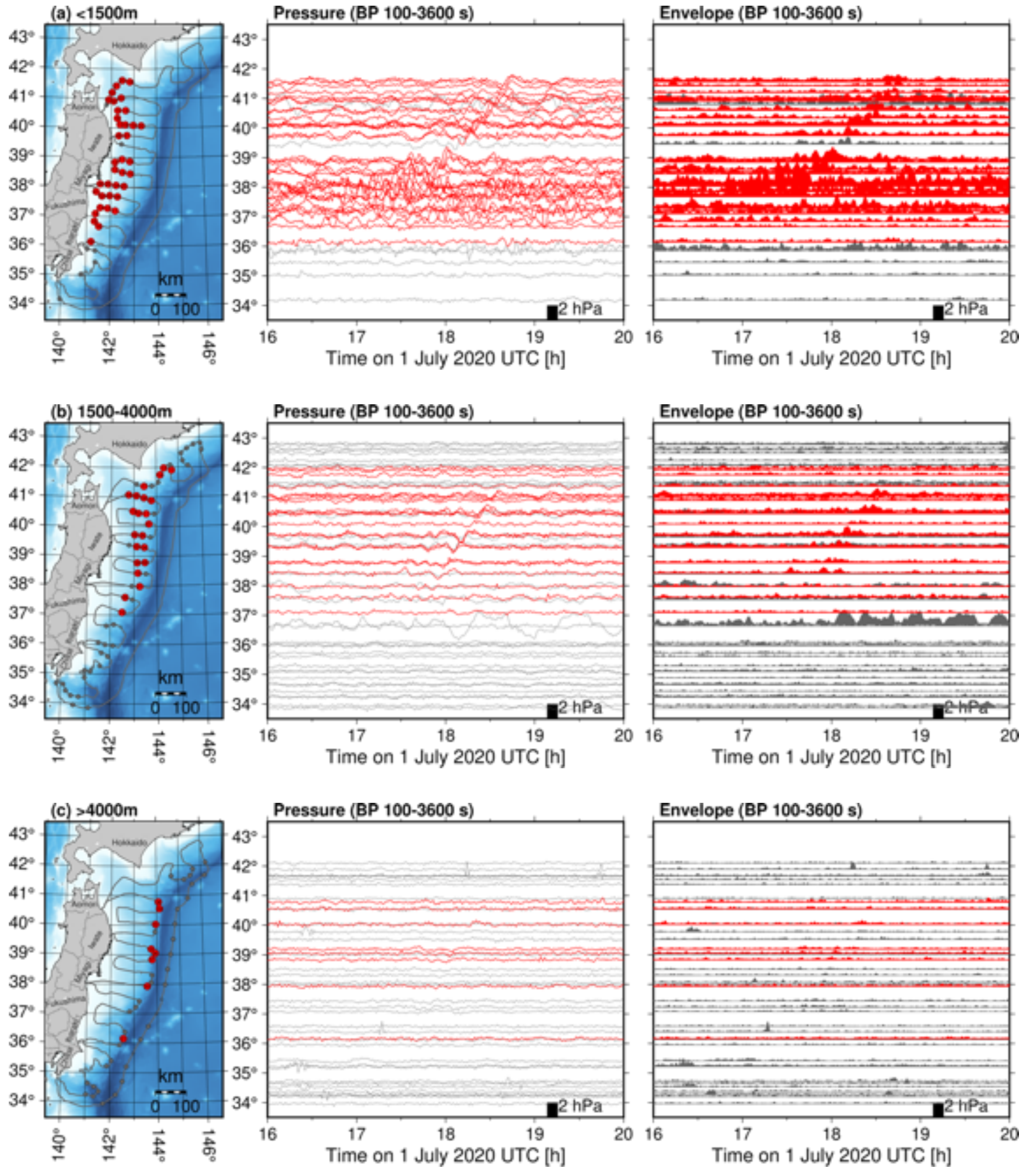

Figure S1. S-net pressure waveforms and envelope waveforms for different water depth bins. Waveforms for the OBPs with depths of (a) < 1500 m, (b) 1500–4000 m, and (c) > 4000 m.

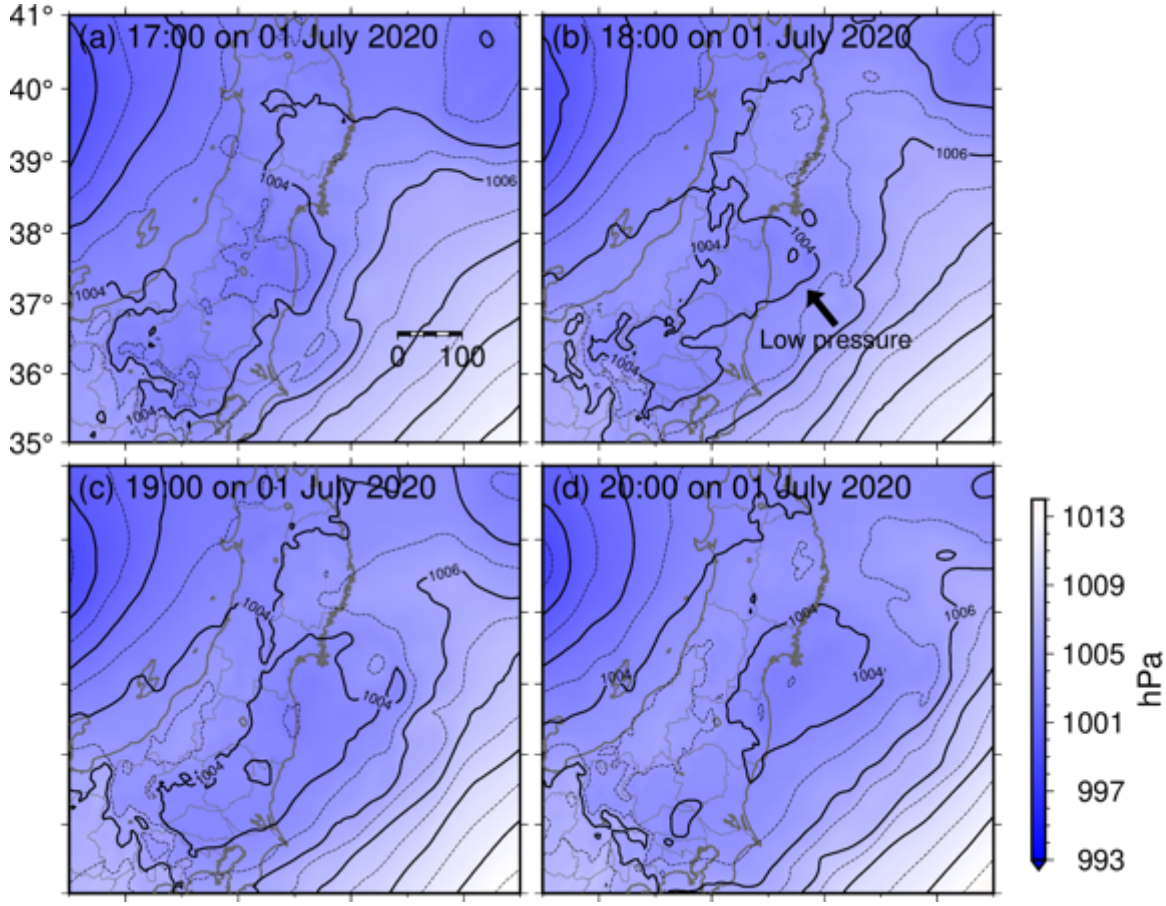

Figure S2. Atmospheric pressure distribution during the meteotsunami. Contour lines are drawn by 1 hPa intervals, and the thick contours are drawn by 2 hPa intervals. The atmospheric low pressure which might be the plausible source of the meteotsunamis is shown by black arrow.

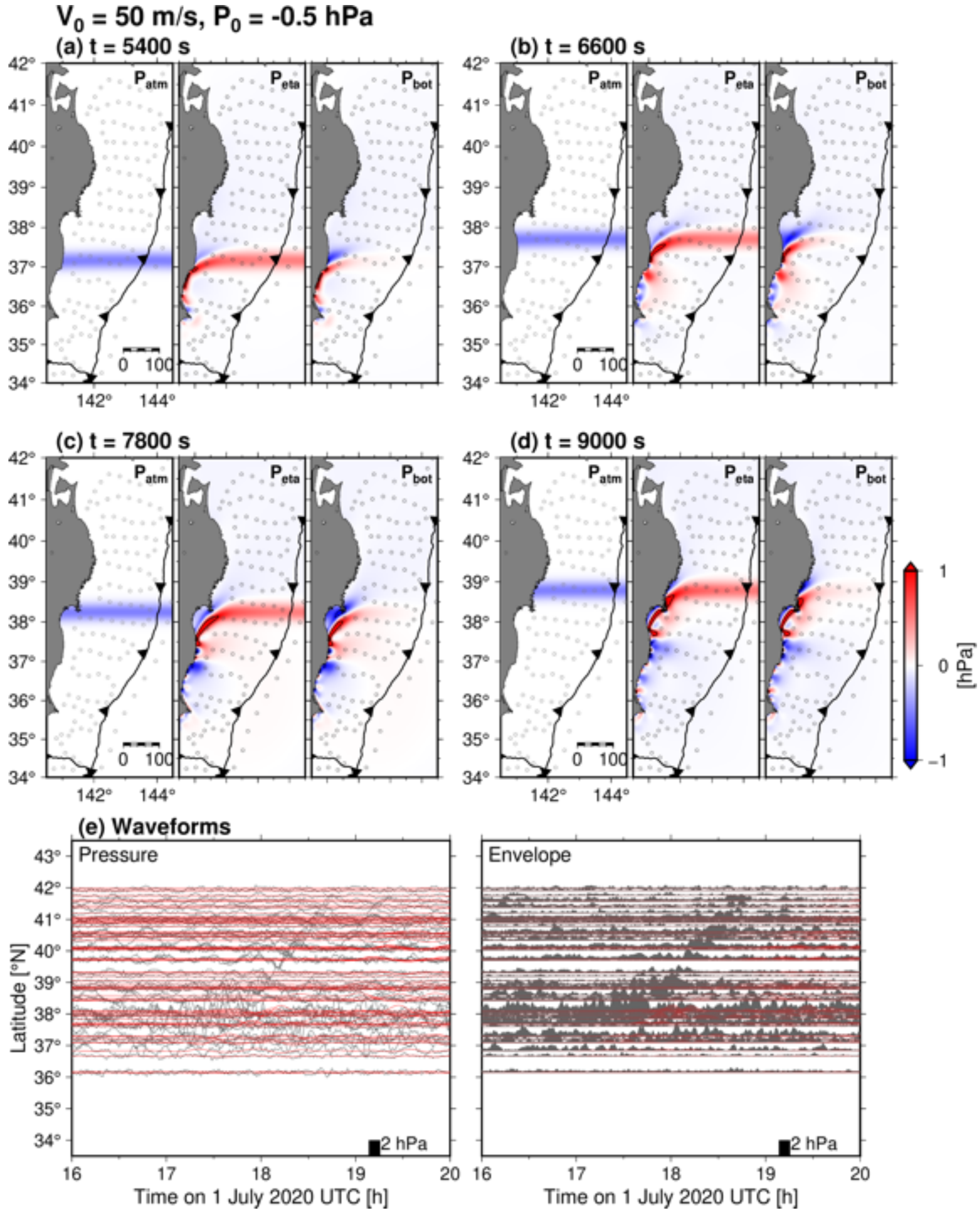

Figure S3. Results of the meteotsunami simulation with V_0 = 50 m/s. See Figure 3 for more detailed explanation of this figure.

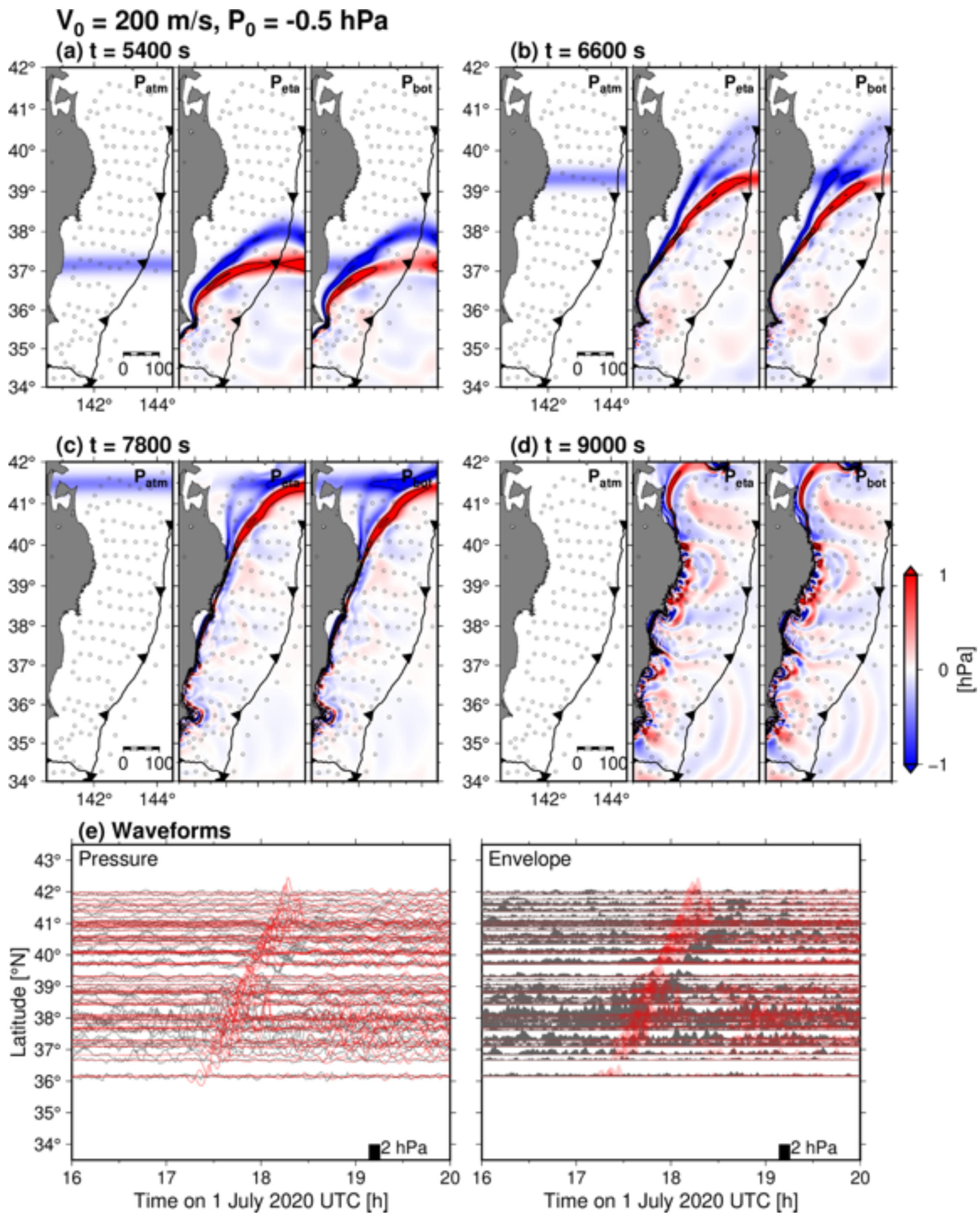

Figure S4. Results of the meteotsunami simulation with V_0 = 200 m/s. See Figure 3 for more detailed explanation of this figure.

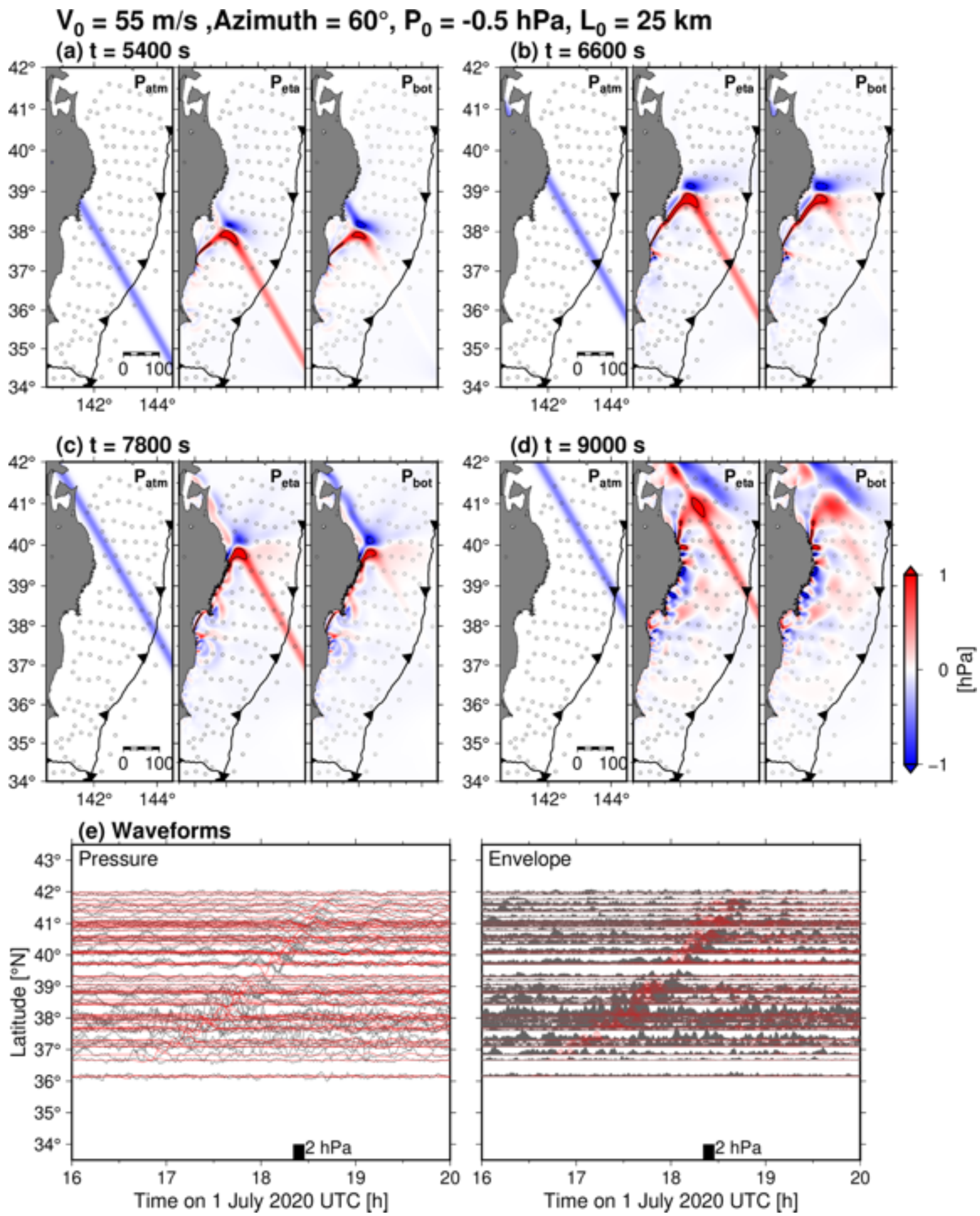

Figure S5. Results of the meteotsunami simulation supposing atmospheric pressure moving to the northeast with V_0 = 55 m/s. See Figure 3 for more detailed explanation of this figure.